*Progress In Electromagnetics Research Letters, Vol. 102, 151–159, 2022*

# Analysis for Six-Pole Outer Rotor Hybrid Magnetic Bearing

**Gai Liu and Huangqiu Zhu***

**Abstract**—In order to solve the nonlinear and coupling problems of three-pole hybrid magnetic bearing, a six-pole outer rotor hybrid magnetic bearing (HMB) is proposed. Firstly, the structure and working principle of the six-pole outer rotor HMB are introduced. Secondly, the linearity and coupling characteristics curves between radial suspension force and control current are analyzed and verified by the finite element method. In comparison with the analysis results of the three-pole HMB, there is no electromagnetic coupling between radial two degrees of freedom of the six-pole outer rotor HMB, and the nonlinear problem of force-current characteristic is solved. Finally, an experimental platform is built. The research results show that the maximum bearing capacity of the six-pole outer rotor HMB is 32.3% higher than that of the three-pole HMB. The suspension force-current characteristic experiment shows that the suspension force-current properties of the six pole outer rotor hybrid magnetic bearing can be considered linear near the equilibrium position, and there is no magnetic coupling between two radial degrees of freedom of the six pole outer rotor HMB near the equilibrium position.

Nomenclature

| | |
|---|---|
| HMB | Hybrid magnetic bearing |
| OSHMB | Outer-rotor six-pole hybrid magnetic bearing |
| THMB | Three-pole hybrid magnetic bearing |
| PM | Permanent magnet |
| DSP | Digital signal processing |
| A11, A12, A21, A22 | Magnetic poles of A phase |
| B11, B12, B21, B22 | Magnetic poles of B phase |
| C11, C12, C21, C22 | Magnetic poles of C phase |
| $F_x$ | The suspension force in the $x$ direction |
| $F_y$ | The suspension force in the $y$ direction |
| $i_x$ | The control current in the $x$ direction |
| $i_y$ | The control current in the $y$ direction |

## 1. INTRODUCTION

The friction between the rotor and stator of a traditional mechanical bearing increases the energy loss, and this can be solved by a magnetic bearing [1]. The traditional magnetic bearings have eight magnetic poles, and four magnetic poles are driven by one power amplifier, so a magnetic bearing requires two power amplifiers [2]. A rotary shaft is supported by two radial magnetic bearings, and the rotary shaft connects with the rotor of a motor [3, 4]. Power amplifier and displacement sensors increase the cost and volume of the magnetic bearing system. Therefore, the compact and cost-effective design has long

---

*Received 10 December 2021, Accepted 7 February 2022, Scheduled 10 February 2022*

* Corresponding author: Huangqiu Zhu (1361322164@qq.com).
The authors are with the School of Electrical and Information Engineering, Jiangsu University, Zhenjiang 212003, China.

been an important issue in research and development of magnetic bearings. One approach is to use sensorless control [5–7]. Only one three-phase inverter is required for three-pole magnetic bearings in [8], which greatly reduces the cost and power consumption of the magnetic bearing system. To increase the stability of magnetic bearings, an accurate mathematical model is established in [9]. Although the three-pole magnetic bearing has many advantages, it also increases the overall design and cost of the system in [10]. A six-pole magnetic bearing is proposed, and the nonlinear and coupling problems of three-pole magnetic bearings are solved [11].

A new six-pole outer rotor hybrid magnetic bearing is put forward. Firstly, the structure and working principle of the six-pole outer rotor hybrid magnetic bearing are introduced, and the mathematical models are deduced. Then, the force-current characteristics and maximum bearing capacity of the three-pole hybrid magnetic bearing and six-pole outer rotor hybrid magnetic bearing are obtained by 3-D FEA analysis, and the data obtained are compared with the theoretical values. Finally, the superiority of the six-pole outer rotor hybrid magnetic bearing is verified by experiments.

## 2. STRUCTURE AND WORKING PRINCIPLE

The six-pole outer rotor hybrid magnetic bearing is mainly composed of permanent magnet, radial stator, rotor, and radial coil, as shown in Figure 1.

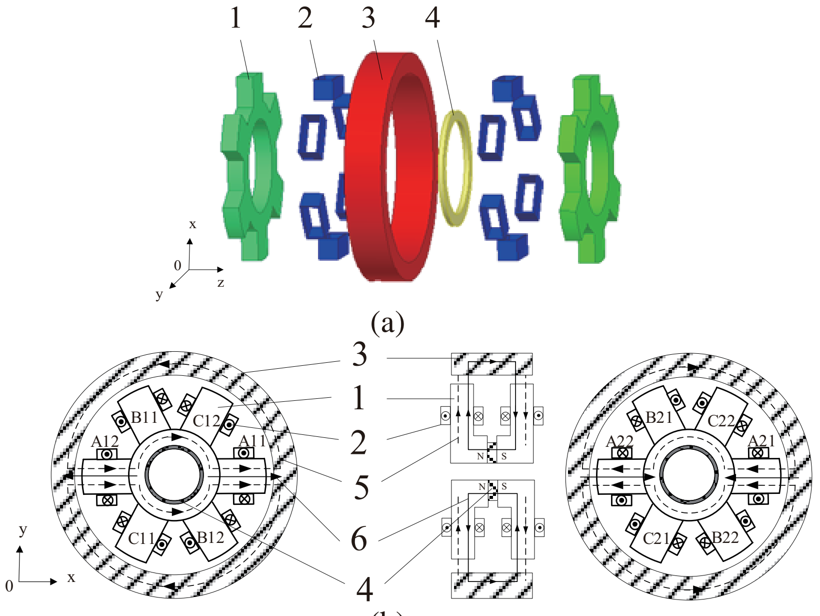

(a)

(b)

**Figure 1.** Structure and magnetic flux paths of six-pole outer rotor hybrid magnetic bearing. (a) 3D model of six-pole outer rotor HMB. (b) Magnetic flux paths of six-pole outer rotor HMB, (1) radial stator, (2) control coils, (3) rotor, (4) PM, (5) control magnetic circuit, (6) permanent magnetic circuit.

There are two kinds of fluxes, bias flux and control flux in the six-pole outer rotor hybrid magnetic bearing. Depicted in Figure 1, the bias flux is generated by the permanent magnet magnetizing along the $z$ direction, and the specific flow direction is from the N pole of the permanent magnet, passing through the left radial stator, left air gap, rotor, right air gap, and right radial stator back to the other pole of the permanent magnet. The control flux is generated by the control coil of each pole and flows only in the side of the corresponding stator. As can be seen from Figure 1(b), there are two stators, and each stator has six magnetic poles. The magnetic poles of the left stator are A11, A12, B11, B12, C11, and C12. The magnetic poles of the right stator are A21, A22, B21, B22, C21, and C22. The magnetic poles A11, A12, A21, and A22 belong to A phase. The magnetic poles B11, B12, B21, and B22 belong to B phase. The magnetic poles C11, C12, C21, and C22 belong to C phase.

When the rotor is not offset, the bias flux at any air gap is equal, and the flow direction is radial. Taking the A phase as an example, the winding modes of A11 and A12 are opposite. When the positive current in the direction shown in Figure 1 enters the A phase, the control flux generated by the control coil is in the same direction as the bias flux. The control flux generated by the control coil of A12 is reverse to the bias flux. The magnetic flux of the magnetic pole A11 is the superposition of two kinds of magnetic flux, and the magnetic pole A12 offsets the two kinds of magnetic flux of the air gap. Therefore, the suspension force between the rotor and magnetic pole A11 will be produced. Similarly, when the negative current enters the A phase, the suspension force is generated along the magnetic pole A12, from the air gap to the magnetic pole. Note that the bias flux flow on the left stator is opposite to that on the right stator, so the coil winding mode of the right stator magnetic pole A21 and the coil winding mode of the left stator magnetic pole A11 are opposite. Each coil winding and working principle of B and C phases are the same. Hence, by changing the value of each phase current, a three-phase inverter can be used to drive the radial two-degree-of-freedom to control the six-pole outer rotor hybrid magnetic bearing.

According to the modeling principle of Maxwell's tensor method, the expression for the Maxwell force of the per unit area d$S$ acting on the rotor at the space angle $\theta$ is:

$$\mathrm{d}F\left(\theta\right)=\frac{B^{2}\left(\theta,t\right)}{2\mu_{0}}\,\mathrm{d}S=\frac{B^{2}\left(\theta,t\right)}{2\mu_{0}}\cdot\left(lr\mathrm{d}\theta\right) \tag{1}$$

where $l$ is the perimeter of the rotor surface, $r$ the rotor diameter, and $\mu_0$ the permeability of vacuum.

When the rotor moves in position due to the interference force $f$, the resultant force $F_s$ of the rotor unit area d$S$ is the Maxwell force plus the interference force $f$, which can be expressed as:

$$\mathrm{d}F_{s}\left(\theta\right)=\mathrm{d}\left(\frac{B^{2}\left(\theta,t\right)S}{2\mu_{0}}+f\right)=\frac{B^{2}\left(\theta,t\right)}{2\mu_{0}}\cdot\left(lr\mathrm{d}\theta\right)+f_{0}\cdot\mathrm{d}S \tag{2}$$

where $f_0$ is the interference force of the rotor unit area d$S$.

The Maxwell force of the rotor is decomposed in two vertical $x$ and $y$ directions:

$$\begin{cases}\mathrm{d}F_{x}\left(\theta\right)=\mathrm{d}F\left(\theta\right)\cos\theta=\frac{B^{2}(\theta,t)lr\cos\theta}{2\mu_{0}}\,\mathrm{d}\theta\\ \mathrm{d}F_{y}\left(\theta\right)=\mathrm{d}F\left(\theta\right)\sin\theta=\frac{B^{2}(\theta,t)lr\sin\theta}{2\mu_{0}}\,\mathrm{d}\theta\end{cases} \tag{3}$$

The magnetic momentum potential generated by the bias magnetic field is

$$F_{1}=H_{m}l_{m} \tag{4}$$

where $H_m$ is the magnetic field strength at the permanent magnet working point, and $l_m$ is the length of the permanent magnet, located along the geomagnetic direction.

If the rotor position is offset at time $t$, the flux density of the biased magnetic field in the gas gap can be expressed as

$$B_{1}\left(\theta,t\right)=F_{1}\cdot\frac{\mu_{0}}{2\delta\left(\theta,t\right)}=\frac{F_{1}\mu_{0}}{2\delta_{r}\left(1-\varepsilon\cos\left(\theta-\alpha\right)\right)} \tag{5}$$

When the rotor is in the equilibrium position, the magnetic flux density amplitude of the biased magnetic field in the air gap can be expressed as

$$B_{1}=\frac{F_{1}\mu_{0}}{2\delta_{r}} \tag{6}$$

The expression for the magnetic flux density is calculated as

$$B_{1}\left(\theta,t\right)=B_{1}\left(1+\varepsilon\cos\left(\theta-\alpha\right)\right) \tag{7}$$

In Equation (7), the air gap magnetic flux density $B_1$ is

$$B_{1}=\frac{\mu_{0}}{2\delta_{r}}\,H_{m}l_{m} \tag{8}$$

The base wave component expression of the gas gap magnetomotive force generated by the rotating magnetic field is

$$F_{2}\left(\theta,t\right)=F_{2}\cos\left(\theta-\omega t-\varphi\right) \tag{9}$$

where $F_2$ is the amplitude of the gas gap magnetic momentum generated by the rotating magnetic field.

When the rotor deviates from equilibrium, the air gap length is

$$\delta\left(\theta, t\right) = \delta_r \left(1 - \varepsilon \cos\left(\theta - \alpha\right)\right) \tag{10}$$

The magnetic flux density produced by the rotating magnetic field at any position of the gas gap can be expressed as

$$B_2\left(\theta, t\right) = F_2\left(\theta, t\right) \cdot \frac{\mu_0}{2\delta\left(\theta, t\right)} = F_2 \cos\left(\theta - \omega t - \varphi\right) \cdot \frac{\mu_0}{2\delta_r\left(1 - \varepsilon\cos\left(\theta - \alpha\right)\right)} \tag{11}$$

The magnetic pole angle is 36°.

$$\begin{cases} F_{2\mathrm{A}},\ \theta \in \left(-\frac{\pi}{10}, \frac{\pi}{10}\right) \\ F_{2\mathrm{B}},\ \theta \in \left(\frac{17}{30}\pi, \frac{23}{30}\pi\right) \\ F_{2\mathrm{C}},\ \theta \in \left(\frac{37}{30}\pi, \frac{43}{30}\pi\right) \\ F_{2\mathrm{a}},\ \theta \in \left(\frac{9}{10}\pi, \frac{11}{10}\pi\right) \\ F_{2\mathrm{b}},\ \theta \in \left(\frac{47}{30}\pi, \frac{53}{30}\pi\right) \\ F_{2\mathrm{c}},\ \theta \in \left(\frac{7}{30}\pi, \frac{13}{30}\pi\right) \end{cases} \tag{12}$$

$$F_2 = \frac{3}{2}F_{2\mathrm{A}} = \frac{3}{2}F_{2\mathrm{B}} = \frac{3}{2}F_{2\mathrm{C}} = \frac{3}{2}F_{2\mathrm{a}} = \frac{3}{2}F_{2\mathrm{b}} = \frac{3}{2}F_{2\mathrm{c}} = \frac{3}{2} \cdot \frac{N_{\mathrm{r}}I}{p} \tag{13}$$

where $N_r$ is the effective turns of the six control coils, $I$ the amplitude of the current, and $p$ the polar log of the rotating magnetic field.

The magnetic density amplitude of the gas gap produced by the control coil is

$$B_2 = \frac{F_2\mu_0}{2\delta_r} = \frac{3}{4} \cdot \frac{\mu_0 N_r}{\delta_r} I \tag{14}$$

Combining Equations (13) and (11),

$$B_2\left(\theta, t\right) = B_2 \cos\left(\theta - \omega t - \varphi\right) \cdot \left(1 + \varepsilon \cos\left(\theta - \alpha\right)\right) \tag{15}$$

The magnetic flux density $B(\theta, t)$ in the gas gap is produced together by the permanent magnet and the control coils, which is expressed as

$$B\left(\theta, t\right) = B_1\left(\theta, t\right) + B_2\left(\theta, t\right) = \left(B_1 + B_2\cos\left(\theta - \omega t - \varphi\right)\right) \cdot \left(1 + \varepsilon\cos\left(\theta - \alpha\right)\right) \tag{16}$$

Therefore, the components of the Maxwell force are

$$\begin{cases} F_x = \int_0^{2\pi} \frac{B^2(\theta,t)\cdot lr\cos\theta \mathrm{d}\theta}{2\mu_0} = \int_{-\frac{\pi}{10}}^{\frac{\pi}{10}} \frac{B^2(\theta,t)\cdot lr\cos\theta \mathrm{d}\theta}{2\mu_0} + \int_{\frac{17}{30}\pi}^{\frac{23}{30}\pi} \frac{B^2(\theta,t)\cdot lr\cos\theta \mathrm{d}\theta}{2\mu_0} \\ \quad + \int_{\frac{37}{30}\pi}^{\frac{43}{30}\pi} \frac{B^2(\theta,t)\cdot lr\cos\theta \mathrm{d}\theta}{2\mu_0} + \int_{\frac{9}{10}\pi}^{\frac{11}{10}\pi} \frac{B^2(\theta,t)\cdot lr\cos\theta \mathrm{d}\theta}{2\mu_0} + \int_{\frac{47}{30}\pi}^{\frac{53}{30}\pi} \frac{B^2(\theta,t)\cdot lr\cos\theta \mathrm{d}\theta}{2\mu_0} + \int_{\frac{7}{30}\pi}^{\frac{13}{30}\pi} \frac{B^2(\theta,t)\cdot lr\cos\theta \mathrm{d}\theta}{2\mu_0} \\ F_y = \int_0^{2\pi} \frac{B^2(\theta,t)\cdot lr\sin\theta \mathrm{d}\theta}{2\mu_0} = \int_{-\frac{\pi}{10}}^{\frac{\pi}{10}} \frac{B^2(\theta,t)\cdot lr\sin\theta \mathrm{d}\theta}{2\mu_0} + \int_{\frac{17}{30}\pi}^{\frac{23}{30}\pi} \frac{B^2(\theta,t)\cdot lr\sin\theta \mathrm{d}\theta}{2\mu_0} \\ \quad + \int_{\frac{37}{30}\pi}^{\frac{43}{30}\pi} \frac{B^2(\theta,t)\cdot lr\sin\theta \mathrm{d}\theta}{2\mu_0} + \int_{\frac{9}{10}\pi}^{\frac{11}{10}\pi} \frac{B^2(\theta,t)\cdot lr\sin\theta \mathrm{d}\theta}{2\mu_0} + \int_{\frac{47}{30}\pi}^{\frac{53}{30}\pi} \frac{B^2(\theta,t)\cdot lr\sin\theta \mathrm{d}\theta}{2\mu_0} + \int_{\frac{7}{30}\pi}^{\frac{13}{30}\pi} \frac{B^2(\theta,t)\cdot lr\sin\theta \mathrm{d}\theta}{2\mu_0} \end{cases} \tag{17}$$

For facilitate calculation, ignoring the square term of $B_2$, the expression is obtained

$$\begin{cases} F_x = \frac{lr}{2\mu_0}\left(\frac{6\pi}{5} B_1 B_2 \cos\varphi + \frac{6\pi}{5}\varepsilon B_1^2 \cos\alpha\right) \\ F_y = \frac{lr}{2\mu_0}\left(\frac{6\pi}{5} B_1 B_2 \sin\varphi + \frac{6\pi}{5}\varepsilon B_1^2 \sin\alpha\right) \end{cases} \tag{18}$$

The expressions for the radial suspension force $F_{ix}$ and $F_{iy}$ controlling the current can be expressed as:

$$\begin{cases} F_{ix} = \frac{3\pi lr\mu_0 H_m l_m N_r}{20\delta_r^2} \cdot \left(\frac{3}{2} I \cos\varphi\right) = \frac{3\pi lr\mu_0 H_m l_m N_r}{20\delta_r^2} i_{xc} \\ F_{iy} = \frac{3\pi lr\mu_0 H_m l_m N_r}{20\delta_r^2} \cdot \left(\frac{3}{2} I \sin\varphi\right) = \frac{3\pi lr\mu_0 H_m l_m N_r}{20\delta_r^2} i_{yc} \end{cases} \tag{19}$$

where $i_{xc}$, $i_{yc}$ are the values of the current in the $x$-axis and the $y$-axis directions in the Clark transformation.

The expression of the Clark transformation is

$$\begin{bmatrix} i_x \\ i_y \end{bmatrix} = \frac{N_r}{N_2} \begin{bmatrix} 1 & -\frac{1}{2} & -\frac{1}{2} \\ 0 & \frac{\sqrt{3}}{2} & -\frac{\sqrt{3}}{2} \end{bmatrix} \begin{bmatrix} i_{\mathrm{A}} \\ i_{\mathrm{B}} \\ i_{\mathrm{C}} \end{bmatrix} \tag{20}$$

In Equation (20)

$$\frac{N_r}{N_2} = \sqrt{\frac{2}{3}} \tag{21}$$

So

$$\begin{bmatrix} i_x \\ i_y \end{bmatrix} = \frac{N_r}{N_2} \begin{bmatrix} i_{xc} \\ i_{yc} \end{bmatrix} \tag{22}$$

$$\begin{bmatrix} i_{xc} \\ i_{yc} \end{bmatrix} = \frac{N_2}{N_r} \begin{bmatrix} i_x \\ i_y \end{bmatrix} \tag{23}$$

Since the total power before and after the transformation is unchanged, 45 Eq. (19) is deformed to

$$\begin{cases} F_{ix} = \frac{3\pi lr\mu_0 H_m l_m N_r}{20\delta_r^2} i_{xc} = \sqrt{\frac{3}{2}} \cdot \frac{3\pi lr\mu_0 H_m l_m N_r}{20\delta_r^2} \cdot i_x \\ F_{iy} = \frac{3\pi lr\mu_0 H_m l_m N_r}{20\delta_r^2} i_{yc} = \sqrt{\frac{3}{2}} \cdot \frac{3\pi lr\mu_0 H_m l_m N_r}{20\delta_r^2} \cdot i_y \end{cases} \tag{24}$$

The plus part of Equation (18) represents the Maxwell force received in the biased magnetic field generated by the permanent magnet when the rotor deviates from the equilibrium position, splitting the expression in the $x$- and $y$-axis directions as

$$\begin{cases} F_{lx} = \frac{lr}{2\mu_0} \cdot \frac{6\pi\varepsilon B_1^2}{5} \cos\alpha = \frac{3\pi lr\varepsilon\mu_0 \cdot H_m^2 l_m^2}{20\delta_r^2} \cdot \cos\alpha = \frac{3\pi lr\mu_0 \cdot H_m^2 l_m^2}{20\delta_r^3} \cdot x \\ F_{ly} = \frac{lr}{2\mu_0} \cdot \frac{6\pi\varepsilon B_1^2}{5} \sin\alpha = \frac{3\pi lr\varepsilon\mu_0 \cdot H_m^2 l_m^2}{20\delta_r^2} \cdot \sin\alpha = \frac{3\pi lr\mu_0 \cdot H_m^2 l_m^2}{20\delta_r^3} \cdot y \end{cases} \tag{25}$$

Since the six-pole radial hybrid magnetic bearing adopts a two-piece structure, the rotor bears twice the Maxwell force of that in the case of a single-piece magnetic bearing.

$$\begin{cases} F_{xx} = 2F_x = 2F_{ix} + 2F_{lx} = \sqrt{\frac{3}{2}} \cdot \frac{3\pi lr\mu_0 H_m l_m N_r}{10\delta_r^2} \cdot i_x + \frac{3\pi lr\mu_0 \cdot H_m^2 l_m^2}{10\delta_r^3} \cdot x \\ F_{yy} = 2F_y = 2F_{iy} + 2F_{ly} = \sqrt{\frac{3}{2}} \cdot \frac{3\pi lr\mu_0 H_m l_m N_r}{10\delta_r^2} \cdot i_y + \frac{3\pi lr\mu_0 \cdot H_m^2 l_m^2}{10\delta_r^3} \cdot y \end{cases} \tag{26}$$

## 3. COMPARATIVE ANALYSIS OF THREE-POLE STRUCTURE AND SIX-POLE STRUCTURE

The difference between the six-pole outer rotor hybrid magnetic bearing and the three-pole outer rotor hybrid magnetic bearing is that the six-pole outer rotor HMB is a symmetric structure.

Figure 2(a) is the magnetic induction intensity distribution of the six-pole outer rotor HMB when the control flux is zero. At the same time, the bias flux of each air gap is 0.4 T, which meets the design requirements. Figure 2(b) is the magnetic induction intensity distribution when the maximum current $i_{\max}$ enters the A phase coil. The maximum magnetic induction intensity of A11 is about 0.8 T, and the magnetic induction intensity of A12 is 0 T. Besides, since the B, C phase currents are both $-0.5i_{\max}$, the magnetic induction intensities of C12 and C11 are 0.6 T and 0.2 T, respectively. This is consistent with the theoretical analysis.

The maximum suspension forces in each direction of the three-pole structure and six-pole structure are compared, as shown in Table 1. The maximum suspension force of the six-pole structure in the $x$ direction is $3B_s^2S/2\mu_0$, and the maximum suspension force of the three-pole structure in the $x$ direction is $9B_s^2S/8\mu_0$. The maximum bearing capacity of the six-pole structure is increased by 33.3% compared with that of the three-pole structure.

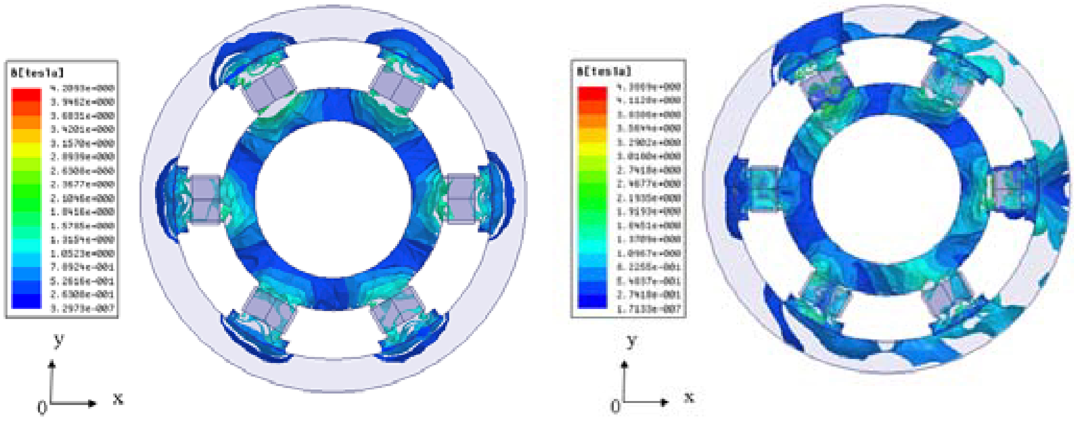

(a) (b)

**Figure 2.** Magnetic flux density. (a) Magnetic density distribution when the control current is 0 A. (b) Magnetic density distribution when the control current is 1 A.

**Table 1.** Maximum suspension force in each direction.

| Bearing capacity direction | Suspension Force of three-pole structure | Suspension Force of six-pole structure |
|---|---|---|
| Positive direction in $x$-axis | $\frac{15B_S^2S}{8\mu_0}$ | $\frac{3B_S^2S}{2\mu_0}$ |
| Negative direction in $x$-axis | $\frac{9B_S^2S}{8\mu_0}$ | $\frac{3B_S^2S}{2\mu_0}$ |
| $y$-axis | $\frac{\sqrt{3}B_S^2S}{\mu_0}$ | $\frac{\sqrt{3}B_S^2S}{\mu_0}$ |

**Table 2.** Parameters of six-pole and three-pole outer rotor HMB.

| Parameters | Three-pole structure | Six-pole structure |
|---|---|---|
| Radial air gap length $l$/mm | 0.5 | 0.5 |
| Saturation induction density $B_S$/T | 0.8 | 0.8 |
| The area of radial magnetic pole $S/\text{mm}^2$ | 640 | 320 |
| The max ampere-turns of radial coils/At | 280 | 140 |
| Magnetomotive force of PM $F_m$/At | 280 | 280 |
| Outer diameter of stator yoke $d_1$/mm | 82 | 82 |
| Inter diameter of stator yoke $d_2$/mm | 58 | 58 |
| Thickness of stator $l_1$/mm | 10 | 10 |
| Outer diameter of rotor $d_3$/mm | 144 | 144 |
| Inter diameter of rotor $d_4$/mm | 118 | 118 |
| Thickness of rotor $l_2$/mm | 23 | 23 |
| Outer diameter of PM $d_5$/mm | 72 | 72 |
| Inter diameter of PM $d_6$/mm | 58 | 58 |
| Axial length of PM $l_3$/mm | 3 | 3 |

The parameters of six-pole outer rotor HMB are designed, and the parameters of three-pole HMB are calculated by that. The parameters are listed in Table 2.

As can be seen from Figure 3 and Figure 4, the relationship curves between the suspension force and the control current of the six pole outer rotor hybrid magnetic bearing vary from the three-pole

HMB. As shown in Figure 3, for three-pole HMB, there is a strong magnetic coupling between the two degrees of freedom; the relationship between the control current $i_x$ and suspension force $F_x$ in the $x$ axis is nonlinear; the relationship between the control current $i_y$ and suspension force $F_x$ in the $x$ axis is nonlinear; the relationship between the control current $i_x$ and suspension force $F_y$ in the $y$ axis is approximate linear; and the relationship between the control current $i_y$ and suspension force $F_y$ in the $y$ axis is approximate linear. As can be seen from Figure 4, for six-pole HMB, there is no magnetic coupling between two degrees of freedom; the relationship between the control current in the $x, y$ direction and the suspension force in the $x$ direction can be regarded as linear; and the relationship between the control current in the $x, y$ axis direction and the suspension force in the $y$ direction can be regarded as linear.

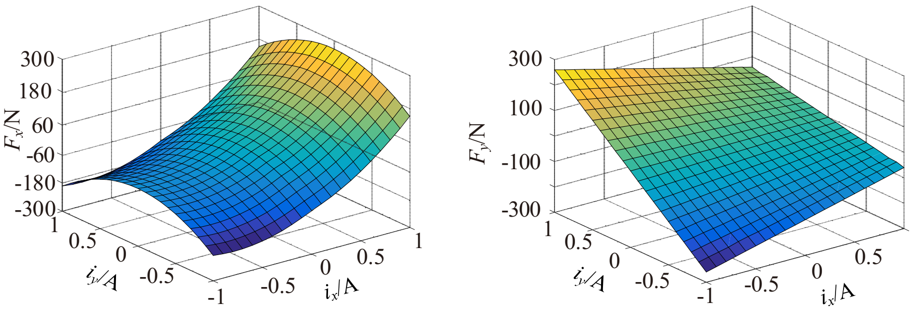

suspension force in the *x* direction suspension force in the *y* direction

**Figure 3.** Relationship curves between radial suspension force and control current of three-pole magnetic bearing.

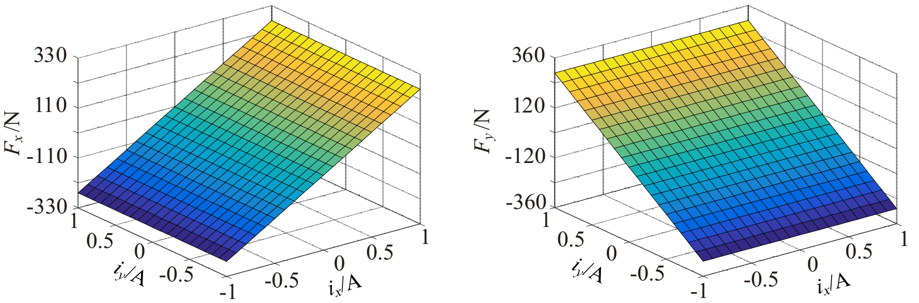

suspension force in the *x* direction suspension force in the *y* direction

**Figure 4.** Relationship curves between radial suspension force and control current of six-pole magnetic bearing.

The above simulation analysis shows that when the rotor is in equilibrium position there is strong magnetic coupling between the two degrees of freedom of the three-pole HMB, but there is no magnetic coupling between two degrees of freedom of six-pole HMB, so the coupling problem of three-pole HMB is solved.

## 4. EXPERIMENT VALIDATION

The experimental platform of the six-pole outer rotor HMB is designed as shown in Figure 5. The experimental platform is mainly composed of eddy current displacement sensors, six-pole hybrid magnetic bearing, regulation circuit, DC voltage source, power drive circuit, AC power supply, upper computer, and DSP controller.

The bearing capacity experiments are carried out. In the suspension force-current characteristic experiment, a large number of experimental data are collected and recorded, and given the extensive

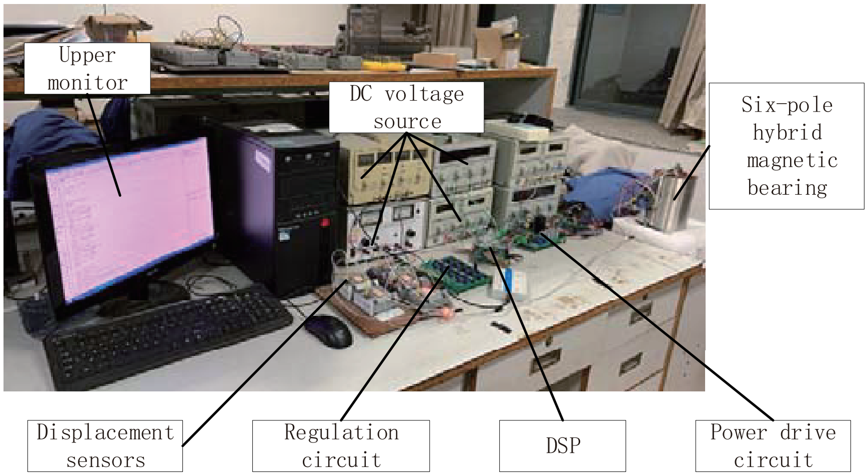

**Figure 5.** Prototype of inverter-fed hybrid magnetic bearing.

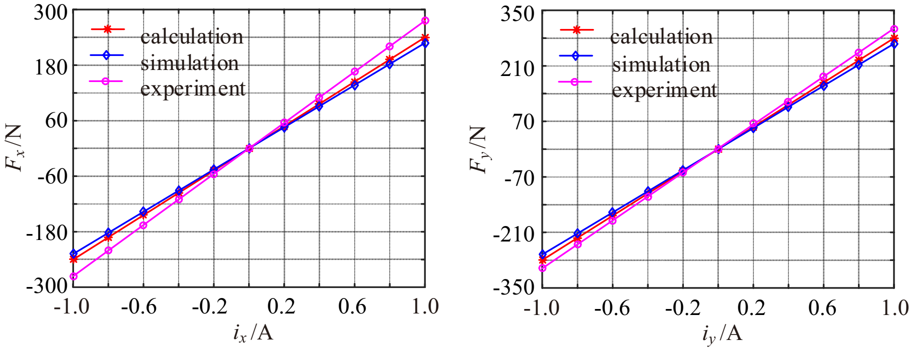

**Figure 6.** Comparison of simulation and experimental results.

**Table 3.** Maximum suspension force compared between the three-pole HMB and the six-pole HMB.

| Bearing capacity direction | Theoretical value (N) | Simulation result (N) | Experiment result (N) |
|---|---|---|---|
| Three-pole HMB | 183 | 181 | 195 |
| Six-pole HMB | 244 | 239 | 258 |

test data and multiple repeated test procedures, the data recorded for each test are for reference only. Using statistical analysis, the data curves compare the finite element results with experimental results clearly. The relationships between suspension force and control current of six-pole HMB are shown in Figure 6. The experimental results agree with the simulated and calculated results very well.

The maximum suspension force of the three-pole HMB is the suspension force in the negative direction of $x$ axis, and the maximum suspension forces are compared between three-pole HMB and six-pole HMB as shown in Table 3. The maximum bearing capacity of the three-pole HMB is 195 N, and the maximum bearing capacity of six-pole HMB is 258 N. Therefore, through the experiment, the maximum bearing capacity of the six-pole HMB is increased by 32.3% compared with the three-pole structure, and the results are close to the theoretical analysis.

## 5. CONCLUSIONS AND DISCUSSION

To solve the nonlinear and coupling problems of the three-pole HMB, a six-pole outer rotor HMB is studied. The simulation results show that the six-pole outer rotor hybrid magnetic bearing has great advantages in both bearing capacity and force-current characteristics. The suspension force-current characteristic experiment shows that the suspension force-current properties of the six pole outer rotor hybrid magnetic bearing can be considered linear near the equilibrium position, and there is no magnetic coupling between two radial degrees of freedom of the six pole outer rotor HMB near the equilibrium position. Under the same conditions, the maximum suspension force of the six-pole outer rotor HMB is 32.3% higher than that of the three-pole HMB.

## ACKNOWLEDGMENT

This work was sponsored in part by the National Natural Science Foundation of China (51675244, 61973144) and Priority Academic Program Development of Jiangsu Higher Education Institutions (PAPD-2018-87).

## REFERENCES

1. Gu, H., H.-Q. Zhu, and Y.-Z. Hua, "Soft sensing modeling of magnetic suspension rotor displacements based on continuous hidden markov model," *IEEE Transactions on Applied Superconductivity*, Vol. 28, No. 3, 1–5, Apr. 2018.
2. Ye, X. and P. Bao, "Finite element analysis of fault tolerance method for eight-pole hybrid magnetic bearing," *2020 IEEE International Conference on Applied Superconductivity and Electromagnetic Devices (ASEMD)*, 1–2, 2020.
3. Usman, I., M. Paone, K. Smeds, and X. Lu, "Radially biased axial magnetic bearings/motors for precision rotary-axial spindles," *IEEE/ASME Transactions on Mechatronics*, Vol. 16, No. 3, 411–420, Jun. 2011.
4. Le, Y. and K. Wang, "Design and optimization method of magnetic bearing for high-speed motor considering eddy current effects," *IEEE/ASME Transactions on Mechatronics*, Vol. 21, No. 4, 2061–2072, Aug. 2016.
5. Peng, C., J. Sun, X. Song, and J. Fang, "Frequency-varying current harmonics for active magnetic bearing via multiple resonant controllers," *IEEE Transactions on Industrial Electronics*, Vol. 64, No. 1, 517–526, Jan. 2017.
6. Gu, H., H. Zhu, and Y. Hua, "Soft sensing modeling of magnetic suspension rotor displacements based on continuous hidden markov model," *IEEE Transactions on Applied Superconductivity*, Vol. 28, No. 3, 1–5, Apr. 2018.
7. Yu, J. and C. Zhu, "A multifrequency disturbances identification and suppression method for the self-sensing AMB rotor system," *IEEE Transactions on Industrial Electronics*, Vol. 65, No. 8, 6382–6392, Aug. 2018.
8. Zhang, W.-Y., H.-Q. Zhu, Z.-B. Yang, X.-D. Sun, and Y. Yuan, "Nonlinear model analysis and "switching model" of AC-DC three degree of freedom hybrid magnetic bearing," *IEEE/ASME Transactions on Mechatronics*, Vol. 21, No. 2, 1102–1115, Apr. 2016.
9. Zhang, W.-Y., H.-K. Yang, L. Cheng, and H.-Q. Zhu, "Modeling based on exact segmentation of magnetic field for a centripetal force type-magnetic bearing," *IEEE Transactions on Industrial Electronics*, Vol. 67, No. 9, 7691–7701, Sept. 2020.
10. Wang, S.-S., H.-Q. Zhu, M.-Y. Wu, and W.-Y. Zhang, "Active disturbance rejection decoupling control for three-degree-of-freedom six-pole active magnetic bearing based on BP neural network," *IEEE Transactions on Applied Superconductivity*, Vol. 30, No. 4, 1–5, Jun. 2020.
11. Liu, G., H.-Q. Zhu, and W.-Y. Zhang, "Principle and performance analysis for six-pole hybrid magnetic bearing with a secondary air gap," *Electronics Letters*, Vol. 57, No. 14, 548–549, 2021.